

# An Improved Observation Model for Super-Resolution Under Affine Motion

Gilles Rochefort, Frédéric Champagnat, *Member, IEEE*, Guy Le Besnerais, and Jean-François Giovannelli

**Abstract**—Super-resolution (SR) techniques make use of sub-pixel shifts between frames in an image sequence to yield higher resolution images. We propose an original observation model devoted to the case of nonisometric inter-frame motion as required, for instance, in the context of airborne imaging sensors. First, we describe how the main observation models used in the SR literature deal with motion, and we explain why they are not suited for nonisometric motion. Then, we propose an extension of the observation model by Elad and Feuer adapted to affine motion. This model is based on a decomposition of affine transforms into successive shear transforms, each one efficiently implemented by row-by-row or column-by-column one-dimensional affine transforms. We demonstrate on synthetic and real sequences that our observation model incorporated in a SR reconstruction technique leads to better results in the case of variable scale motions and it provides equivalent results in the case of isometric motions.

**Index Terms**—Affine motion, bspline, convex regularization, inverse problems,  $L_2$  approximation, multipass interpolation, projection, super-resolution.

## I. INTRODUCTION

**S**UPER-resolution (SR) techniques aim at estimating a high-resolution image with reduced aliasing from a sequence of low-resolution (LR) frames. The literature on the subject is abundant—see [1]–[6] and [7] for a recent review.

Our contribution deals with the class of “reconstruction based” SR techniques [8], which can be split in three steps: 1) estimation of inter-frame motion; 2) computation of a linear observation model including motion; and 3) regularized inversion of the linear system.

We are interested in aerial imaging applications which often imply nonisometric motion, as in the case of an airborne imager getting closer to the observed scene—see Section VI-C. Such nonisometric motion fields can be estimated using various registration algorithms [9], [10]. Hence, step 1) is not the main issue in this context. Concerning step 2), the SR literature is rather allusive: most published methods implicitly assume translational

motion [1], [4], [6], [8], [11]–[19]. To the best of our knowledge, if some former contributions apply to affine [20], [21] or even homographic [9], [22] warps none of them explicitly deals with variable distance from scene to imager in step 2).<sup>1</sup> So, we focus on the construction of a proper observation model for affine motions with consistent scale changes.

Section II proposes a bibliographical survey of the SR literature, with respect to the observation model. It is shown that published methods are not adapted to the considered context: its main difficulty is to account for nontranslational motion in a tractable discrete model.

Section III is devoted to the proposed new observation model that extends the popular one introduced by Elad and Feuer [5] by replacing traditional pointwise interpolation by techniques based on  $L_2$  approximations and shifted bspline basis [23]. We show that our model leads to a more precise prediction of LR frame pixel values, in the case of a combined zoom and rotation motion.

Further comparisons are performed on SR reconstruction results. Section IV briefly introduces the convex regularization framework that we use for SR reconstruction. Such techniques are customary in various inverse problems, including restoration and SR [2], [5], [24].

We use the resulting SR reconstruction technique to compare various observation models on synthetic (Section V) and real (Section VI) datasets. These experiments consistently show that our model is more accurate and reliable for sequences combining rotation and important scale changes, at the expense of a moderate increase of computational load.

## II. ANALYSIS OF PREVIOUS WORKS

This section describes several published observation models differing by the way they account for motion through numerical approximations.

### A. Notations

Uppercase letters (respectively, boldface letters) refer to matrices (respectively, vectors).  $\mathbf{n} = [n, l]^t \in \mathbb{Z}^2$  and  $\mathbf{i} = [i, j]^t \in \mathbb{Z}^2$  denote discrete positions of LR and SR pixels and  $\mathbf{u} = [u, v]^t \in \mathbb{R}^2$  denotes real positions on the image plane. An image  $x$  can be described by a continuous field  $x(\mathbf{u})$ , or by a sequence of discrete coefficients  $x[\mathbf{i}]$  and as lexicographically ordered vector  $\mathbf{x}$ .

### B. General Observation Model

Let  $x(\cdot)$  be the input irradiance field and  $y[\cdot]$  be the observed LR image.  $y$  is a sampled version of the convolution of  $x$  with

<sup>1</sup>It is addressed formally in [3] but not implemented nor demonstrated.

Manuscript received February 25, 2005; revised April 11, 2006. The associate editor coordinating the review of this manuscript and approving it for publication was Prof. Stanley J. Reeves.

G. Rochefort is with Realeyes 3D-France, Saint-Cloud, France (e-mail: grochefort@realeyes3d.com).

F. Champagnat and G. Le Besnerais are with Office National d'Etudes et de Recherches Aérospatiales (ONERA), 92322 Chatillon Cedex, France (e-mail: frederic.champagnat@onera.fr; guy.lebesnerais@onera.fr).

J.-F. Giovannelli is with Laboratoire des Signaux et Systèmes, Supélec, Plateau de Moulon, 91192 Gif-sur-Yvette Cedex, France (e-mail: giovannelli@lss.supelec.fr).

Color versions of Figs. 1, 2, 3, 8, and 9 are available online at <http://ieeexplore.ieee.org>.

Digital Object Identifier 10.1109/TIP.2006.881996

an optical point spread function (PSF)  $h_o$  integrated by a box function  $I$  corresponding to the collecting surface of the detector

$$y[\mathbf{n}] = \int_{\mathbb{R}^2} (h_o * x)(\mathbf{n}\Delta - \mathbf{v}) I(\mathbf{v}) d\mathbf{v}$$

with  $\mathbf{n} \in \mathcal{G}_\Delta$ .  $\mathcal{G}_\Delta \subset \mathbb{Z}^2$  is the set of discrete detectors positions on a grid with step  $\Delta$ . Let us denote  $N = \text{Card}(\mathcal{G}_\Delta)$  the number of LR pixels in frame  $y$ .

It is customary to define a joint optics-plus-detector PSF  $h = h_o * I$  so that  $y[\mathbf{n}] = h * x(\mathbf{n}\Delta)$ .

SR methods rely on the usual ‘‘brightness constancy’’ assumption which is the basis of many motion estimation techniques, in particular intensity-based techniques [10]. In this framework, SR methods assume that temporally neighboring frames originate from a unique input  $x$  up to a warp modeling relative sensor/scene motion.

Let  $y_k (k = 1, \dots, K)$  denote a neighboring frame of  $y$ , then: i)  $y_k$  derives from an irradiance field  $x_k$  through sensor  $h : y_k[\mathbf{n}] = h * x_k(\mathbf{n}\Delta)$  and ii) there is a warp  $w_k$ , such that  $x_k(\mathbf{u}) = x(w_k(\mathbf{u}))$ . Combination of both equalities yields

$$y_k[\mathbf{n}] = h * (x \circ w_k)(\mathbf{n}\Delta). \quad (1)$$

The next step is discretization of  $x$  for the sake of numerical computations. The irradiance field  $x$  is decomposed on a shifted kernel basis

$$x(\mathbf{u}) = \sum_{\mathbf{i} \in \mathcal{G}_{\Delta'}} x[\mathbf{i}] \varphi(\mathbf{u} - \mathbf{i}\Delta'). \quad (2)$$

where  $\mathcal{G}_{\Delta'}$  is the SR grid, with step  $\Delta'$  and  $M = \text{Card}(\mathcal{G}_{\Delta'})$  is the number of SR pixels. The ratio  $L = \Delta/\Delta'$  defines the practical magnification factor (PMF) of the SR process: it is usually greater than two. Note that it does not imply that the actual resolution improvement is as high as the PMF.

$\varphi$  may be any classical interpolation kernel (box function, bilinear, ...). In the sequel, we use bspline basis, which encompass most classical interpolation schemes [25]–[27]. Then  $\varphi$  is a separable bspline kernel of order  $m : \varphi(\mathbf{u}) = \beta^m(u)\beta^m(v)$ , where  $\beta^m(u)$  is the  $(m+1)$ -fold convolution of a box function.

Let us rewrite (1) as

$$y_k[\mathbf{n}] = \int_{\mathbb{R}^2} x(w_k(\mathbf{v})) h(\mathbf{n}\Delta - \mathbf{v}) d\mathbf{v}. \quad (3)$$

Injecting (2) yields

$$y_k[\mathbf{n}] = \sum_{\mathbf{i} \in \mathcal{G}_{\Delta'}} a_k[\mathbf{n}, \mathbf{i}] x[\mathbf{i}],$$

$$a_k[\mathbf{n}, \mathbf{i}] = \int_{\mathbb{R}^2} \varphi(w_k(\mathbf{v}) - \mathbf{i}\Delta') h(\mathbf{n}\Delta - \mathbf{v}) d\mathbf{v}. \quad (4)$$

Using lexicographically ordered vector representation of images, a matrix formulation writes

$$\mathbf{y}_k = \mathbf{A}_k \mathbf{x}.$$

The whole matrix  $\mathbf{A} = [\mathbf{A}_1 \dots \mathbf{A}_K]^t$  is huge with dimensions  $KN \times M$ ,  $M \approx NL^2$ . For instance, a sequence of  $K = 10$  frames, with dimensions  $N = 128^2$  and a PMF  $L = 2$  leads to about 43 billion elements. Of course,  $\mathbf{A}_k$  is a sparse matrix with a band structure, as practical PSF  $h$  spreads over two or three LR pixels at most and  $\varphi$  is a separable bspline kernel, whose support is  $(m+1)\Delta'$  wide. However, the cost of computing all nonzero elements of  $\mathbf{A}$  remains formidable for general warps  $w_k$ .

In the following, we review landmark SR papers with respect to the way they compute  $\mathbf{A}$ . We discuss three main approaches:

- 1) exact computation for special cases of  $w_k$ ,  $h$  and  $\varphi$ ;
- 2) *convolve-then-warp* approximation;
- 3) *warp-then-convolve* approximation.

### C. Exact Computation

Exact computation is tractable only in two special cases:

- motion is a global translation;
- $\varphi$  and  $h$  are both box functions and motion is affine.

1) *Global Translation*: When  $w_k$  is a global translation, (1) leads to a simple convolution. Indeed, replacing  $w_k(\mathbf{u}) = \mathbf{u} - \boldsymbol{\tau}_k$  inside (4) yields

$$a_k[\mathbf{n}, \mathbf{i}] = \varphi * h(\mathbf{n}\Delta - \mathbf{i}\Delta' - \boldsymbol{\tau}_k)$$

and the observation equation writes

$$y_k[\mathbf{n}] = \sum_{\mathbf{i}} \varphi * h(\mathbf{n}L\Delta' - \mathbf{i}\Delta' - \boldsymbol{\tau}_k) x[\mathbf{i}]$$

$$= g_k * x[\mathbf{n}L]$$

with  $g_k(\mathbf{u}) = (\varphi * h)(\mathbf{u}\Delta' - \boldsymbol{\tau}_k)$ . For a given integer  $L$ , each LR frame appears as a subsampled version of the discrete convolution of  $x$  with kernel  $g_k$ .

Most of the early SR literature is devoted to this global translation case. It naturally leads to either Fourier techniques [1], [11], [12] or equivalent multichannel filtering techniques [13] based on the generalized Papoulis theorem [28].

2)  *$\varphi$  and  $h$  Are Box Functions*: When  $\varphi$  and  $h$  are box functions [2], [3], [29], (4) is the common area between each detector and each warped SR pixel (see Fig. 1).

Such an observation model has been proposed by Stark and Oskoui for rotational warps [29]. No indication is provided in their paper about the numerical computation of the relevant intersections.

Assuming affine motion, each warped SR pixel is a convex polygon, and computation of the intersection of two convex polygons can be performed by a ‘‘clipping’’ algorithm such as [30]. However, this technique is not suitable for SR purpose due to its high computational burden.

### D. Convolve-Then-Warp

Let us start back from (3). In practice,  $h$  scarcely spreads over two or three LR pixels, thus integral (3) extends on a neighbor-

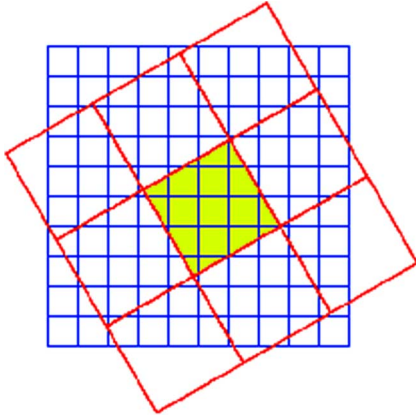


Fig. 1.  $\varphi$  and  $h$  are assumed box functions and motion is a rotation. The fine grid represents the grid of SR pixels, while the coarse one is the grid of detectors. Common areas between the middle detector and each SR pixel are colored.

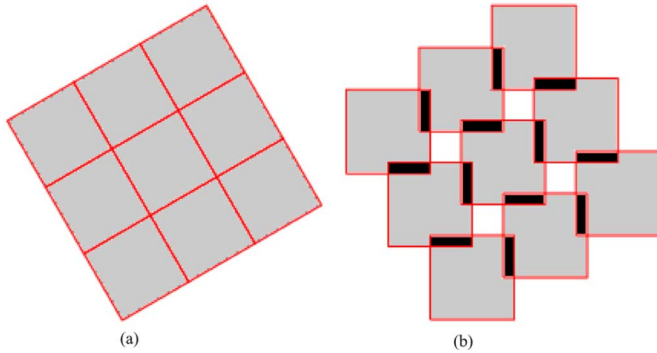


Fig. 2. Illustration of the Convolve-then-Warp approximate model (5): white regions are not accounted for, gray ones are integrated even while black regions are incorrectly integrated in two detectors output. (a) Correct detector integration area. (b) Local translation approximation of the warp and resulting detector area.

hood  $\mathcal{V}(\mathbf{n}\Delta)$  around  $\mathbf{n}\Delta$ . Let us assume that  $w_k(\mathbf{u})$  can be locally approximated by a translation

$$w_k(\mathbf{u}) \approx w_k(\mathbf{n}\Delta) + \mathbf{u} - \mathbf{n}\Delta, \quad \mathbf{u} \in \mathcal{V}(\mathbf{n}\Delta).$$

Then (3) can be approximated by a convolution

$$y_k[\mathbf{n}] \approx (h * x)(w_k(\mathbf{n}\Delta)). \quad (5)$$

Such an approximation is depicted in Fig. 2. The center of each detector is well positioned, but the integration area is a rough approximation. Such an approximation leads to errors in the integration step for large rotations and scale variations.

The discretization of this model is much easier than the general model (1), because it is an irregular sampling of a convolution. The simple model of Schultz and Stevenson [2] is a special case of this approach when  $h$  and  $\varphi$  are both box functions and the detector center positions are rounded to integer multiples of  $\Delta'$ . Then, the components  $a_k[\mathbf{n}, \mathbf{i}]$  are binary, with  $a_k[\mathbf{n}, \mathbf{i}] = 1$  if the  $\mathbf{i}$ th SR pixel is inside the  $\mathbf{n}$ -th detector area, approximated as in Fig. 2(b). A refined version of this model is used in [31].

As a conclusion, this model appears computationnally attractive but is clearly unable to correctly account for nontranslational warps because of the fixed detector geometry (see Fig. 2).

### E. Warp-Then-Convolve

This approach consists in using the convolution relationship (1) between the data  $\mathbf{y}_k$  and the warped SR image  $x_k(\mathbf{u}) = x(w_k(\mathbf{u}))$ . If a discretized version  $\hat{x}_k$  of  $x_k$  over the  $\Delta'$ -shifted basis functions  $\varphi$  is available, (1) can easily be discretized as

$$\mathbf{y}_k = \mathbf{D}\mathbf{H}\hat{\mathbf{x}}_k$$

where  $\mathbf{D}$  is a down-sampling matrix, and  $\mathbf{H}$  is the convolution matrix associated to the optical-plus-detector response.

Now the main problem is to construct  $\hat{\mathbf{x}}_k$  using the discretized SR image coefficients  $x[\cdot]$  defined by (2). A first approach may be to enforce equality on the grid nodes

$$\sum_{\mathbf{i} \in \mathcal{G}_{\Delta'}} \hat{x}_k[\mathbf{i}] \varphi((\mathbf{l} - \mathbf{i})\Delta') = \sum_{\mathbf{j} \in \mathcal{G}_{\Delta'}} x[\mathbf{j}] \varphi(w_k(\mathbf{l}\Delta') - \mathbf{j}\Delta').$$

If  $\varphi$  is a bspline of order  $m = 0$  or  $m = 1$ , it satisfies  $\varphi((\mathbf{l} - \mathbf{i})\Delta) = \delta(\mathbf{l} - \mathbf{i})$ , and we get

$$\hat{x}_k[\mathbf{l}] = \sum_{\mathbf{j} \in \mathcal{G}_{\Delta'}} x[\mathbf{j}] \varphi(w_k(\mathbf{l}\Delta) - \mathbf{j}\Delta). \quad (6)$$

In other words, the discrete coefficient  $\hat{x}_k[\mathbf{l}]$  is the interpolation of  $x$  at point  $w_k(\mathbf{l}\Delta)$ . If  $\varphi$  is a box function ( $m = 0$ ), (6) reduces to nearest neighbor interpolation and if  $\varphi$  is a triangle function ( $m = 1$ ), (6) is a bilinear interpolation.

Interpolation (6) leads to the definition of a warping matrix  $\mathbf{W}_k$ , which summarizes all motion information. The complete image formation model is then

$$\mathbf{y}_k = \mathbf{D}\mathbf{H}\mathbf{W}_k\mathbf{x}. \quad (7)$$

This is exactly the formulation proposed by Elad and Feuer [5], [21] referred to as the ‘‘E&F’’ model in the following.

Fig. 3 summarizes this method: starting from the sought SR image Fig. 3(a), an intermediate high-resolution image Fig. 3(b) is constructed with a pixel grid aligned with the detector grid using either bilinear or nearest neighbor interpolation. Integration and subsampling are then straightforward.

Compared to the previous approach, the E&F model seems much more precise for rotation warps. However, one can foresee aliasing problems in the case of scale changes due to the pointwise interpolation step (6).

## III. PROPOSED OBSERVATION MODEL

This section introduces an original observation model extending the E&F model, by replacing pointwise interpolation (6) by a technique based on  $L_2$  function approximation.

Dealing with variable scale using  $L_2$  approximation technique is not easy in 2-D. In this context, Catmull and Smith [32]

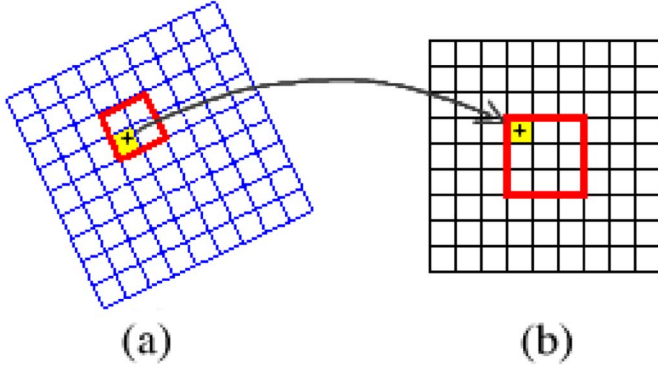


Fig. 3. Illustration of the E&F model: starting from SR image Fig. 3(a), an intermediate high-resolution image Fig. 3(b) is constructed with a pixel grid aligned with the  $y_k$  data detector grid using either bilinear or nearest neighbor interpolation.

introduced an efficient decomposition of 2-D affine transforms into separable 1-D transforms.

First, we will introduce such a decomposition into our observation model. Next, we focus on the 1-D operations in order to achieve a  $L_2$  approximation on a bspline basis. Finally, we will compare observation models and point out the improvements provided by the proposed model.

#### A. Warping Decomposition

Thevenaz and Unser showed that 2-D invertible affine transforms can be handled by two-shear or three-shear decompositions [23]. Each shear is a vertical or horizontal coordinate transform such as

$$S_u(\mathbf{u}) = \begin{pmatrix} \alpha_2 & \beta_2 \\ 0 & 1 \end{pmatrix} \begin{pmatrix} u \\ v \end{pmatrix} + \begin{pmatrix} \varepsilon_2 \\ 0 \end{pmatrix} \quad (8)$$

$$S_v(\mathbf{u}) = \begin{pmatrix} 1 & 0 \\ \beta_1 & \alpha_1 \end{pmatrix} \begin{pmatrix} u \\ v \end{pmatrix} + \begin{pmatrix} 0 \\ \varepsilon_1 \end{pmatrix}. \quad (9)$$

Both of them are 1-D affine transforms separately applied row-by-row or column-by-column. As an example, Fig. 4 provides the intermediate images resulting of each shear of the following affine motion and decomposition

$$\begin{pmatrix} 1 & 1/4 \\ -1/4 & 7/16 \end{pmatrix} = \begin{pmatrix} 1 & 0 \\ -1/4 & 1/2 \end{pmatrix} \begin{pmatrix} 1 & 1/4 \\ 0 & 1 \end{pmatrix}. \quad (10)$$

This decomposition is not unique, and the choice of one particular decomposition impacts the transformed image quality. Catmull and Smith [32] mentioned the bottleneck problem resulting from a down-scaling in one pass followed by up-scaling in the next pass, resulting in a loss of resolution.

Many approaches have been proposed to minimize image degradation, depending on the considered transform. For instance, Paeth [33] has proposed a three-shear decomposition well-suited for rotation. Other authors refer to  $N$ -pass decomposition [34].

Multipass interpolation techniques and their limitations are outside the scope of this article, the reader can refer to [34] for deeper insight. In the sequel, we consider only two-shear decompositions. In this case, there are two possibilities, and one

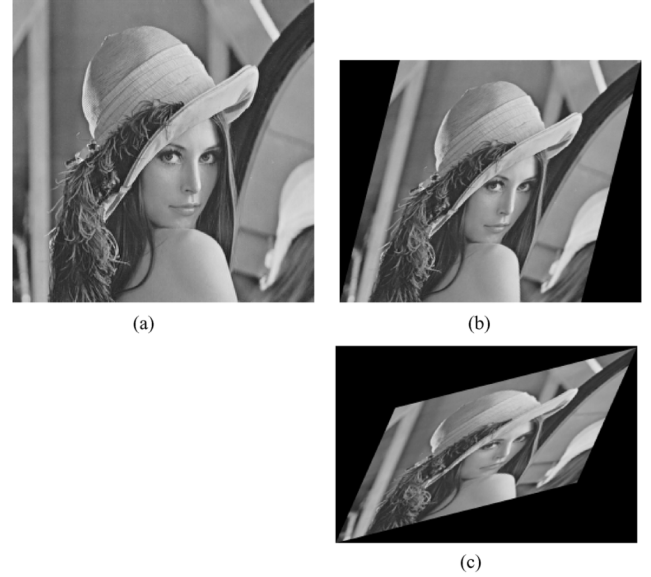


Fig. 4. Example: the affine transform of (10) is decomposed in two steps. Each step is a shear along one coordinate image axis. (a) Original image. (b) Horizontal shear. (c) Vertical shear.

selects the decomposition which reduces the involved scale variations [23], [35], [36].

#### B. One-Dimensional Affine Transform Approximation

Let us consider a 1-D affine transform with parameters  $(a, \tau) : f(u) \rightarrow f((u - \tau)/a)$ . With this notation,  $a < 1$  yields a signal reduction and  $a > 1$  yields a signal magnification. It is clear that signal reduction may result in important discretization errors (as naive subsampling undergoes a frequency aliasing).

In the line of Thevenaz *et al.* [23], let us decompose  $f$  on the 1-D shifted bspline basis:

$$f(u) = \sum_{k \in \mathcal{G}_Q} f[k] \beta^m(u - k) \quad (11)$$

where  $\mathcal{G}_Q \subset \mathbb{Z}$  denotes the set of  $Q$  discrete samples (for instance the set of pixels of a row of the image). We search for coefficients  $g[k], k \in \mathcal{G}_Q$  such that  $g$ , defined by

$$g(u) = \sum_{k \in \mathcal{G}_Q} g[k] \beta^m(u - k) \quad (12)$$

achieves the best approximation of  $f((u - \tau)/a)$  in the  $L_2$  sense, i.e., minimization of  $\int [f((u - \tau)/a) - g(u)]^2 du$ . The approximation is the orthogonal projection, and the optimal coefficients satisfy the orthogonality equations

$$\left\langle g(u) - f\left(\frac{u - \tau}{a}\right), \beta^m(u - k) \right\rangle = 0 \quad (13)$$

for  $k \in \mathcal{G}_Q$ . Replacing (11) and (12) in (13) yields

$$\sum_j g[j] \beta^{2m+1}[j - k] = \sum_l f[l] a \xi_a^m(k - \tau - al)$$

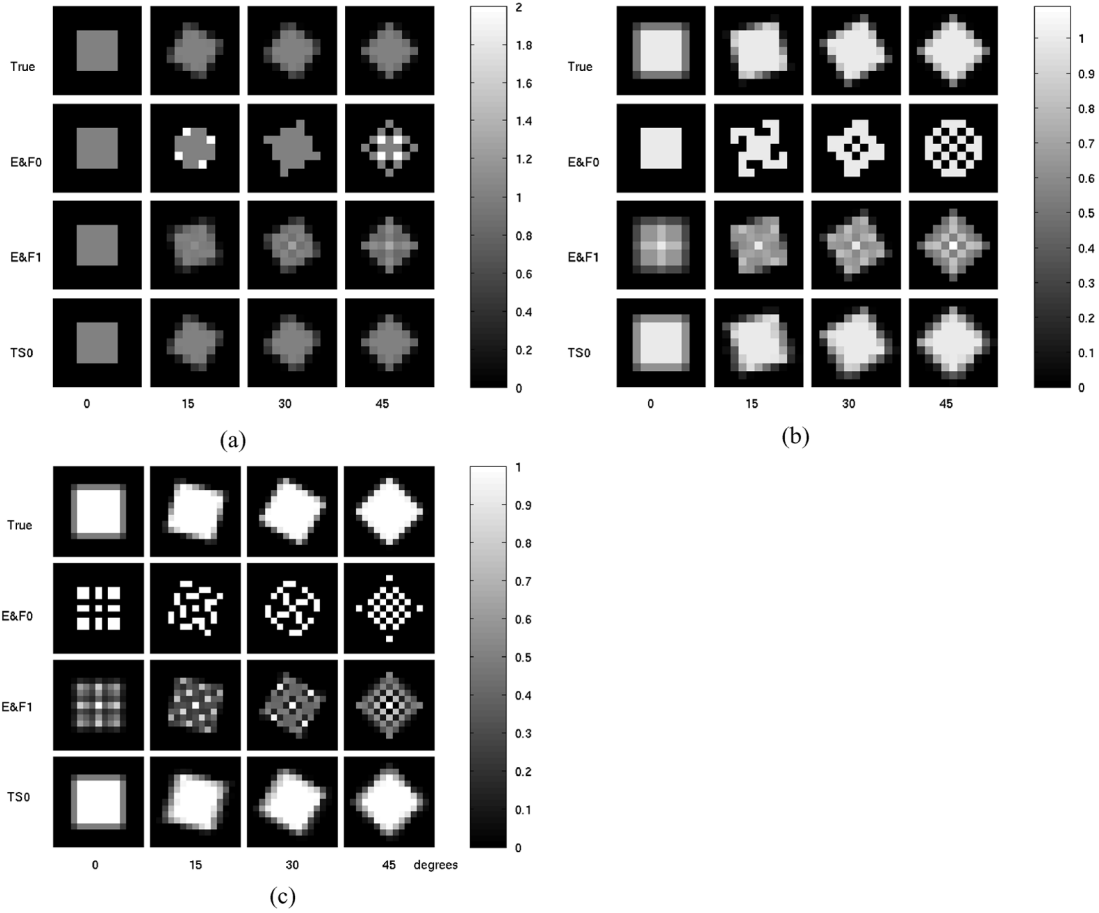


Fig. 5. Comparing observation models: SR pixels contributions to one detector. Scale factor (a) 1.0, (b) 1.2, and (c) 1.6, rotation up to 45°. The models being compared come from the E&F methods with order 0 (E&F0) and order 1 (E&F1) interpolation. The last line shows the proposed TS0 model, while the first line shows the true contributions. (a) Scale factor 1. (b) Scale factor 1.2. (c) Scale factor 1.6.

with  $\beta_a^m(u) = \beta^m(u/a)/a$  and  $\xi_a^m = \beta_a^m * \beta^m$ . The so-called bi-kernel  $\xi_a^m$  encodes the geometric transform of a sample to a different scale space [36], and actually provides an optimal anti-aliasing filter [37]. If  $a \neq 1$ ,  $\xi_a^m$  is not a bspline kernel, but remains a piecewise polynomial. A closed-form expression of  $\xi_a^m$  is provided in [35].

Finally, the sought coefficients  $g[k]$  write

$$g[k] = (\beta^{2m+1})^{-1} * \left( a \sum_{l \in \mathcal{G}_Q} f[l] \xi_a^m(k - \tau - al) \right) \quad (14)$$

and the inverse filter  $(\beta^{2m+1})^{-1}$  can be efficiently implemented through recursive filtering [27].

To sum up the process, given a sequence of signal samples  $f(k)$  and 1-D affine transform parameters  $(a, \tau)$  the approximation goes through four steps:

- 1) compute bspline coefficients  $f[k]$ ;
- 2) compute the bi-kernel function  $\xi_a^m$ ;
- 3) compute  $g[k]$  with (14);
- 4) post-filter coefficients  $g[k]$  to get samples values  $g(k)$ .

*Remark 1:* The first and the last steps are not required when the bspline representation order  $m$  is 0 or 1. Indeed, for these particular orders, bspline coefficients are identical to image samples.

*Remark 2:* In the translation case ( $a = 1$ ),  $\xi_a^m(u) = \beta^{2m+1}(u)$ . The  $L_2$  approximation then turns to a mere bspline interpolation with a higher order kernel.

### C. Two-Shear Observation Model

In the proposed model, the  $k$ th observed frame  $\mathbf{y}_k$  (in vector notation) writes

$$\mathbf{y}_k = \text{DHS}_k^1 \text{S}_k^2 \mathbf{x},$$

where  $\text{S}_k^1$  and  $\text{S}_k^2$  are shear operators. Each operator is an 1-D row-by-row (or column-by-column) affine transform, which is implemented as described in the previous section. In the sequel, we use an order-0 bspline kernel. Thus, as a consequence of Remark 2, our model is identical to that of Elad and Feuer with bi-linear interpolation for translation motion. The resulting model is denoted TS0 for the two-shear model with 0-order bspline basis.

### D. Comparing Observation Models

In this section, we illustrate the quality of each observation model compared to exact computation in the special case of  $h$  and  $\varphi$  chosen as box functions and affine motion—see Section II-C.

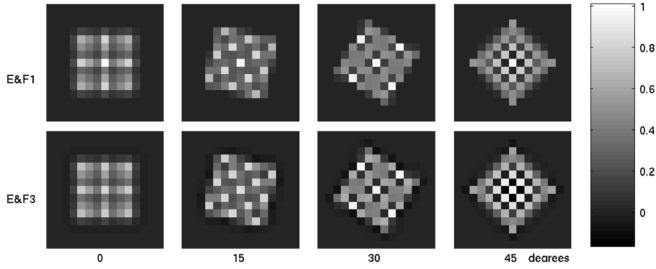


Fig. 6. Comparing E&F1 model with an Elad and Feuer model with bicubic interpolation (E&F3). Scale factor 1.6 and rotation up to  $45^\circ$ .

We represent the components of the observation matrix  $a_k[\mathbf{n}, \bullet]$  for a unique LR pixel in the form of an image patch. This patch displays the weighting coefficients actually applied on SR image pixels for computing one LR detector output. The first rows of the following three arrays of patches show the exact components for rotation angles  $\{0^\circ, 15^\circ, 30^\circ, 45^\circ\}$ , scale variations of 1 [Fig. 5(a)], 1.2 [Fig. 5(b)], and 1.6 [Fig. 5] and a PMF of 5.

The remaining patches show the approximated components obtained using Elad and Feuer models with nearest neighbor interpolation (E&F0) or with bilinear interpolation (E&F1) and the proposed model (TS0).

The Convolve-then-Warp model is not presented, but would lead to the same image patch made of a fixed size square pattern, whatever rotation and zoom factor.

Fig. 5 shows that E&F0 is always incorrect even with limited rotations and/or scale variations. It is noticeable that in Fig. 5(a), some coefficients value reach two: some SR pixels (white colored) contribute twice to the detector. Such a behavior has been previously observed for the ‘‘Convolve-then-Warp’’ approach—see Fig. 2. In the same time, several SR pixels do not contribute at all to the detector.

E&F1 provides a better approximation. Still, contributions of SR pixels are not uniform inside the detector footprint. This is already observed in Fig. 5(a) with rotations, and takes more importance in Fig. 5(b) and Fig. 5(c) with scale factor and rotations. As E&F1 contributions appear as a smoothed version of E&F0 ones, one wonders if a bicubic interpolation (E&F3) would give correct contributions. This is not the case, as shown by Fig. 6. Moreover, as bicubic interpolation does not preserve positivity, the E&F3 model exhibits negative contributions.

Whatever the interpolation method, Elad and Feuer models become inaccurate for rotations as low as  $15^\circ$  and a zooming factor as low as 20%.

In contrast, the TS0 observation model ensures that the contributions of SR pixels are uniform inside the detector footprint whatever rotation and/or scale factor being applied. Remaining differences between exact contributions and TS0 ones are located on the detector boundaries: TS0 contributions spread on slightly more than true ones.

#### IV. REGULARIZATION FRAMEWORK

The inversion step is tackled within a classical convex regularization framework [24] as in many other SR methods [2],

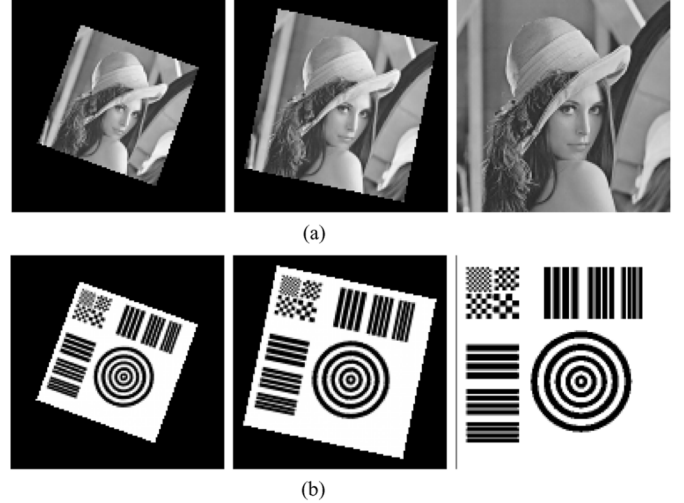


Fig. 7. First, middle, and last frame of sequences (a) *Lena* and (b) *Mire*.

[5]. The estimated SR image is the (possibly constrained) minimizer of a regularized criterion based on observation model and convex edge-preserving penalty

$$J_\lambda(\mathbf{x}) = \sum_k \|\mathbf{y}_k - \mathbf{A}_k^{\text{model}} \mathbf{x}\|^2 + \lambda \sum_{c \in \mathcal{C}} \psi_s(\mathbf{v}_c^t \mathbf{x}). \quad (15)$$

The first term of criterion (15) is a least-squares discrepancy between data and model output:  $\mathbf{A}_k^{\text{model}}$  stands for the observation model which is to be inverted and derives either from the Elad and Feuer approach or from the proposed model of Section III. The second term is a convex penalization term [24].  $\mathcal{C}$  is the set of cliques: it consists of all subsets of three adjacent pixels either horizontal, vertical, and diagonal.  $\mathbf{v}_c$  denotes a second-order difference operator within clique  $c$ . The regularization parameter  $\lambda$  balances the trade-off between the two terms of the criterion. The potential  $\psi_s$  is chosen as a  $L_2 - L_1$  hyperbolic function

$$\psi_s(u) = 2s(\sqrt{s^2 + u^2} - s).$$

Parameter  $s$  sets the threshold between the quadratic behavior ( $u \ll s$ ), which allows small pixel differences smoothing and the linear behavior ( $u \gg s$ ) aimed at preserving edges. The latter part produces a lower penalization of large differences compared to a pure quadratic function.  $\psi$  has the same qualitative behavior as the Huber function of [2].

Finally, for a given observation model, four solutions are computed, based on:

- quadratic penalty;
- quadratic penalty and positivity constraint;
- hyperbolic penalty;
- hyperbolic penalty and positivity constraint.

The criterion is convex by construction and has a unique global minimizer. The optimization can be achieved by iterative gradient-like techniques [38] and we resort to a limited memory BFGS algorithm.<sup>2</sup> It belongs to the class of Quasi-Newton

<sup>2</sup>The implementation named VMLMB, has been provided by É. Thiébaud (thiebaut@obs.univ-lyon1.fr).

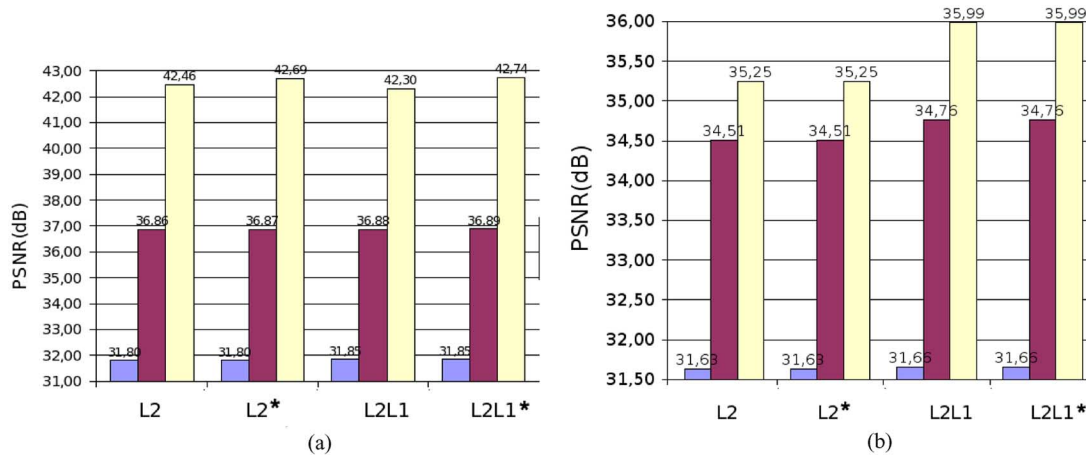


Fig. 8. SR performances on the *Lena* sequence. Three observation models [E&F0 (cyan), E&F1 (magenta), and TS0 (yellow)] and four criteria are compared. Solutions which use a positivity constraint are labelled with a star. (a) No additional noise. (b) Additive Gaussian noise of variance 2.

algorithms which only requires evaluation of the criterion and its gradient (no second-order derivative is explicitly needed) and it is known to have better convergence properties than gradient algorithms.

## V. EXPERIMENTS WITH SYNTHETIC SEQUENCES

This section presents the experiments conducted on synthetic sequences. Using synthetic sequences has two main advantages.

- Sequences are built from a reference HR image which will later be used as a reference to compare with reconstructed SR images.
- We control all imaging parameters: noise level, PSF, and image size. Motion is exactly known too.

### A. Synthetic Data

To generate a sequence of LR frames, the observation matrices  $A_k$  are computed exactly according to assumptions of Section II-C that  $\varphi$  and  $h$  are box functions. As previously said, such a technique is very time consuming.

We simulate a smooth motion with a rotation up to  $20^\circ$  and a zoom factor up to 1.6. Each frame is  $128 \times 128$  and is built from a  $256 \times 256$  HR reference image. In Fig. 7(a), we show the first, middle, and last frame generated from the reference HR image *Lena*.

We also generate another sequence from a bitonal calibration pattern named *Mire*. The first, middle, and last image of the sequence are shown in Fig. 7(b).

### B. Results

Four regularized solutions and three observation models (E&F0, E&F1, and TS0) are then available. Hence, we finally compare performances of 12 SR settings with respect to the reference HR image, by means of the PSNR (peak signal-to-noise ratio,  $\text{PSNR} = 20 \log_{10}(255/\sqrt{e})$ , with  $e$  the mean square error). For each setting, the presented result is obtained with the best regularization parameter (i.e., selected to get the highest reachable PSNR).

Let us first deal with the “Lena” sequence of Fig. 7(a). Fig. 8(a) sums up the performance levels which have been achieved. First note that, on these relatively smooth images,

various regularization settings lead to similar performances, and unconstrained quadratic regularization suffices to obtain good results. But we observe strong differences between observation models. On the average, there is an improvement from 4 dB (noisy case) up to 6 dB (no noise) between the E&F0 and the E&F1 models. Moreover, there is also a gain of 1 to 6 dB between the E&F1 model and the TS0 model.

Fig. 10 illustrates the differences between reconstructed SR images, using  $L_2 - L_1$  regularization and positivity constraint, depending on the chosen observation model. Once again, the reconstructed images shown on the first row of Fig. 10 have been obtained with the best regularization parameters. The E&F reconstructions are slightly more blurred than the SR image obtained from the proposed TS0 model. This is confirmed in the lower row which shows image error with respect to the reference HR image: the TS0 observation model yields a better reconstruction on high frequency areas, like the feather on the hat or the eyes.

We have also measured CPU time on a Pentium 4 at 2.66 GHz. For this particular sequence, one iteration duration is respectively 2.0 and 4.6 s, for E&F0 and E&F1 methods. Our model requires 5.9 s per iteration. All methods converge roughly with the same number of iterations. Hence, our method is 30% more time consuming than E&F1.

We now consider the bitonal “Mire” sequence shown in Fig. 7(b). Results are reported in Fig. 9 in terms of PSNR. As expected, this high-frequency sequence leads to much stronger differences between regularization terms and constraints.

As previously, strong differences are observed between observation models. On the average, there is a gain improvement from 5 dB (noisy case) up to 10 dB (no noise) between E&F1 model and TS0. Such an improvement is due to the high contrast in *Mire* image. Indeed, we know from Section III-D that our observation model does not induce nonhomogeneous contributions in the case of variable scale motion. The induced errors in the reconstructions are more visible in high-contrast areas—see Fig. 11 compared to Fig. 10.

We also note that, in the noiseless case, hyperbolic regularization does not improve performances of E&F methods, whereas we notice a gain up to 1 dB on the average, with the TS0 model.

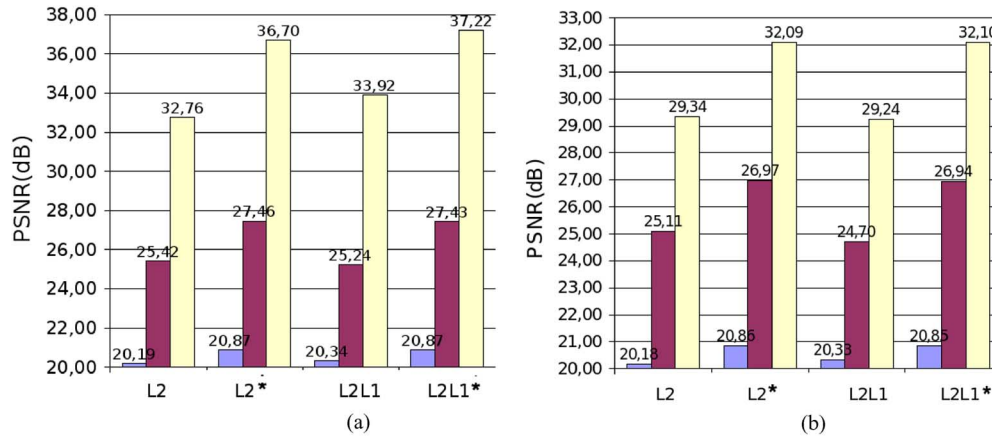


Fig. 9. SR Performances on sequence *Mire*. Three observation models [E&F0 (cyan), E&F1 (magenta), and TS0 (yellow)] and four criteria are compared. Positivity constraint is labelled with a star. (a) No additional noise. (b) Gaussian noise of variance 2.



Fig. 10. First Row: reconstructed SR images. From left to right: E&F0, E&F1, and TS0 observation model. All reconstructions are performed with a hyperbolic regularization and positivity constraint. Second row: differences between HR reference image and reconstructed SR images.

E&F reconstructions are much more noisy than the one obtained with the TS0 model. Let us recall that these reconstructions are obtained with a regularization parameter adjusted to get the better PSNR w.r.t. the reference HR image. The selected regularization parameter is lower ( $10^{-4}$ ) with the TS0 model than with E&F models ( $10^{-3}$ ). This might indicate that the more precise the model is the less it is necessary to regularize. In other words, regularization compensates for model errors which are lower with the proposed TS0 model.

By using synthetic sequences with rotational and variable scale motion, we have shown that the TS0 observation model leads to better reconstructed SR images than E&F methods, whatever the regularization involved.

As a general comment, it should be emphasized that performances are much more sensitive to a change of observation model than to a change of regularization. In other words, a good choice of the observation model leads to much higher improve-

ment than changing the regularization term, at least in the context of rotation and scale variation explored here.

## VI. EXPERIMENTS ON REAL SEQUENCES

In this section, we compare observation models on real sequences. We first discuss prior assumptions on the sequences with an emphasis on motion modelization and estimation, then we present the results obtained on two real datasets.

### A. General Assumptions and Motion Estimation

SR requires the knowledge of the sensor response and of the motion field between frames. We use the common box function model for the PSF. Note that all the tested observation models can accommodate a more general PSF.

We restrict our experiments to affine motion between frames, since the proposed TS0 model is limited to these motion fields. Affine model accurately describes the motion of a planar scene

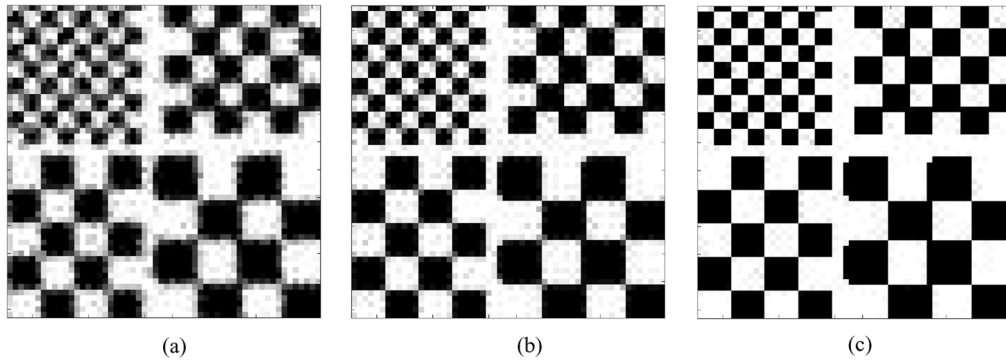


Fig. 11. Top-left parts of SR reconstructed images with hyperbolic regularization and positivity constraint. (a) E&F0 model. (b) E&F1. (c) Proposed TS0 model. Parameters have been adjusted to get the best PSNR w.r.t. HR reference image.

through orthographic projection [39]. Such assumptions are usually not valid on the whole field of view (except in special purpose experiments—see Section VI-B, nevertheless the affine motion model is often a good local approximation of complex motion fields [9], valid in a restricted part of the image support (see an example in the aerial sequence of Section VI-C).

We focus on sequences which exhibit large affine motions, with total zoom factor greater than 1.4 and rotations higher than  $20^\circ$  (with inter-frame zoom up to 1.2 and rotation  $5^\circ$ ). Note that such experimental settings are not considered in the previous papers on SR, even those which address the nontranslational context [9], [22].

The first problem is to register each image of the sequence with respect to the reference image (usually the more resolved one). In this context, direct intensity based methods, which minimize a DFD (displaced frame difference) criterion are subject to false local minima, even using a multiresolution approach. This is due to the sensitivity of DFD criterion with respect to large rotational and scale changes. Hence, we use a two-step approach:

- 1) compute a rough affine motion from scale-invariant keypoints matching;
- 2) refine the affine model using multiresolution DFD minimization on a restricted part of the image.

The first step uses scale-invariant fast transform (SIFT) keypoints of Lowe [40]. We match hundreds of keypoints between the considered frame and the reference one by SIFT descriptor correlation, then we robustly fit an affine model on selected matches using a crude rejection threshold. The second step is essentially a domestic version of the pyramidal image registration method of Thevenaz *et al.* [10].

*B. Lab Tests*

We made several SR experiments by using sequences of a bitonal resolution chart printed on an A4 paper sheet observed with a AVT-046B SVGA Marlin B/W camera. We acquired image sequences with variable inter-frame translation, rotation and zoom factor: some examples are shown in Fig. 12. Each frame of a sequence is registered with respect to the reference frame as explained in the previous section. We ran SR reconstructions with the three concurrent observation models and quadratic or hyperbolic regularization, subject to positivity

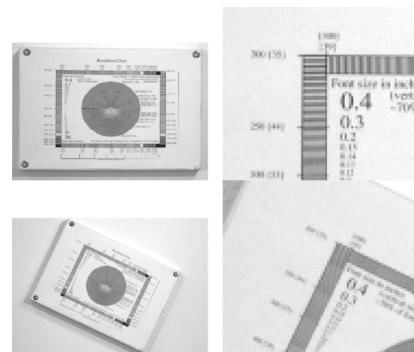


Fig. 12. Sample of frames of the resolution chart, for various rotations and zoom factors. Left column: Zoom on the region used for further SR comparison. Top: Reference frame, which is the most resolved one.

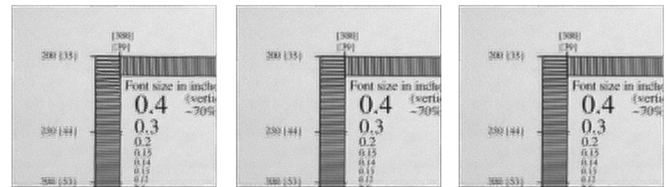


Fig. 13. Reconstruction results with PMF  $L = 3$  using seven frames with global translation motion, in an under-regularized quadratic setting,  $\lambda = 7 \cdot 10^{-3}$ . From left to right: E&F0, E&F1, and TS0 models.

constraint. For each setting, several values of the regularization parameter have been tried. Indeed, most of the time there is a certain range of (low) values of the parameter where differences between methods can easily be observed, whereas above some regularization strength, all methods become equivalent and yield an oversmoothed result.

As a first example, we process a purely translational sequence, using seven frames with a PMF  $L = 3$  and a quadratic regularization: comparison on a small ( $240 \times 240$ ) region is shown in Fig. 13, for a low value of  $\lambda = 7 \cdot 10^{-3}$ . As expected, in this case E&F1 and TS0 lead to quasi-identical results (PSNR = 68 dB) whatever the parameter  $\lambda$ , while E&F0 shows some instability for low  $\lambda$ .

Figs. 14 and 15 compared SR results on seven frames of a sequence with both rotation (up to  $25^\circ$ ) and zoom (there is a factor 1.5 between the reference image and the farthest view). We use either quadratic regularization (upper part of the figures)

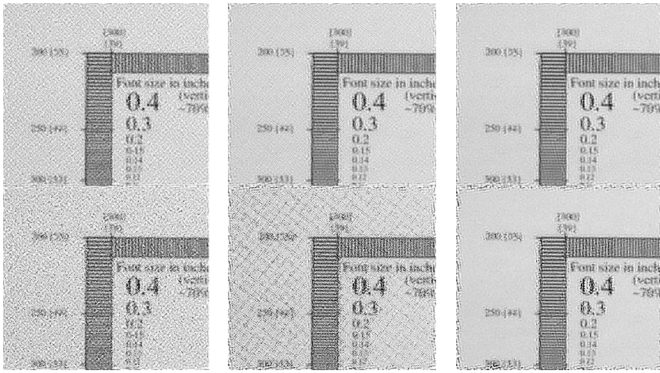


Fig. 14. Reconstruction results with PMF  $L = 3$  using seven frames with zoom and rotations, in an under-regularized setting. Top: Quadratic regularization,  $\lambda = 10^{-3}$ . Bottom: Hyperbolic regularization,  $s = 10, \lambda = 3.10^{-3}$ . From left to right: E&F0, E&F1, and TS0 models.

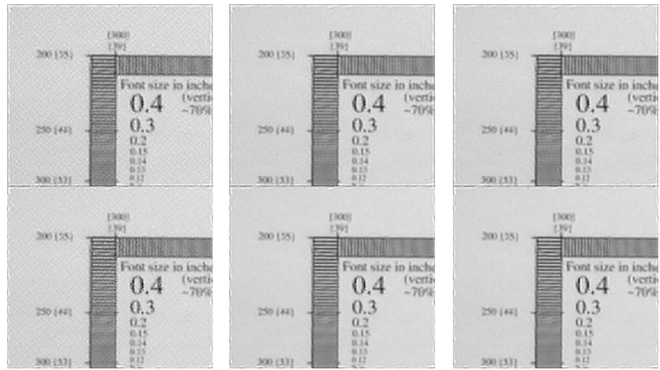


Fig. 15. Reconstruction results with PMF  $L = 3$  using seven frames with zoom and rotations, using a balanced regularization strength. Top: Quadratic regularization,  $\lambda = 10^{-2}$ . Bottom: Hyperbolic regularization,  $s = 10, \lambda = 3.10^{-2}$ . From left to right: E&F0, E&F1, and TS0 models.

or hyperbolic regularization with a threshold parameter  $s = 10$  (lower part).

For a low value of the regularization parameter ( $\lambda = 10^{-3}$  with quadratic term and  $\lambda = 3.10^{-3}$  with hyperbolic regularization), see Fig. 14. E&F0 and E&F1 suffer from artifacts in the form of a pseudo-periodic texture, which is of high amplitude in E&F0 and less important, but manifest, in E&F1. Not surprisingly, this phenomenon is amplified by the hyperbolic regularization. For the same regularization parameter, TS0 does not encounter such instabilities, but exhibits ripples which are typical of an under-regularized quadratic solution, and appear amplified by the hyperbolic edge-preserving potential.

For a more balanced value of the regularization parameter, see Fig. 15; E&F0 is still clearly degraded by instabilities. E&F1 and TS0 are now very close, but a careful examination of both solutions reveals that small amplitude artifacts remain in the E&F1 reconstruction.

### C. Aerial Sequence

Fig. 16 displays the first and the last frames of an infrared sequence captured by an array sensor mounted on an airborne platform. As the plane gets closer to the scene, the last frame is the most resolved one and is chosen as the reference frame.



Fig. 16. IR sequence captured by an airborne sensor. Motion results from variable distance and small rotation. (a) First frame. (b) Last frame.



Fig. 17. Detail of the last (reference) frame. Lined-up cans zoomed up twice using bilinear interpolation. The cans are not resolved. The black vertical line in the lower middle of the image is the antenna on the building seen in Fig. 16.

The scene is a harbor with the sea and waterfront in the foreground, a building with a vertical antenna in the middle and a series of cans lined up in the background. Two ships are present in the right low part of the last frame. Because of perspective effects—the lowest part of the frame is closer to the sensor than the upper part—apparent motion is closer to an homography than an affinity. From the first frame to the reference one, the lower part (respectively, upper part) of the field of view is magnified with a factor about 1.4 (respectively, 1.6). Therefore, our method can only be applied to small regions of the frames.

Two regions are considered in the sequel: 1) in the upper part of the scene, the lined-up cans that remain unresolved in the reference frame (see Fig. 17) and 2) in the right lower part of the scene, the waterfront and the ships—see Fig. 20.

We considered five frames of the sequence, Fig. 16 displays two of them. As already described, motion is estimated using SIFT on the whole sequence then the intensity based method of [10] is used to refine the SIFT estimate in each region.

SR reconstruction is performed with the algorithms of Section V-A, with quadratic regularization ( $s = \infty$ ) and positivity constraint. PMF  $L = 2$  along both image axis.

### D. Upper Region

The observation models are compared through the SR reconstructions in Fig. 18.

The image quality in Fig. 18 gradually increases from the top image (E&F0) to the bottom image (TS0 model). Even if the latter is still not a high quality image, the improvement in resolution enables the count of the right block of cans in the bottom image, whereas it is less obvious in the middle image, and even impossible in the upper image. The results of Fig. 18 look somewhat oversmooth. So a lower regularization parameter has been tested; results are displayed in Fig. 19.

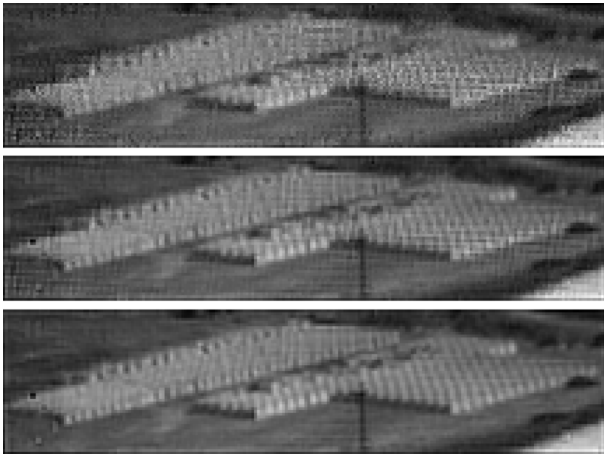


Fig. 18. Reconstructions obtained through E&F0 (top image), E&F1 (middle image) and TS0 (bottom image) observation model.  $\lambda = 5 \cdot 10^{-3}$ .

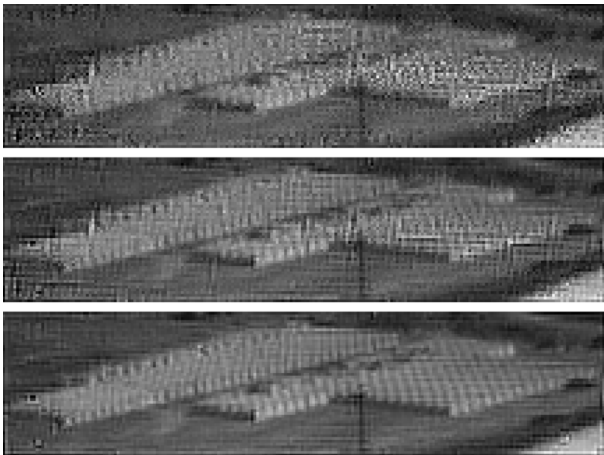


Fig. 19. Reconstructions obtained through E&F0 (top image), E&F1 (middle image), and TS0 (bottom image) observation model.  $\lambda = 1 \cdot 10^{-3}$ .



Fig. 20. Detail of the last frame of Fig. 16. Lower right part of the scene: waterfront and ships zoomed up twice using bicubic interpolation.

Fig. 19 reveals that E&F0 and E&F1 are severely affected by the decrease of the regularization parameter, whereas our model seems more robust: artifacts appear in the right upper part of the scene, but cans can still be counted.

*E. Right Lower Region*

Fig. 21 proposes similar results for the ships at the right lower part of the scene. The ships appear in bright contrast. A bicubic interpolation of the last observed frame is provided in Fig. 20.

The top image (E&F0 model) in Fig. 21 has many localized high-frequency artifacts, part of them are absent in the

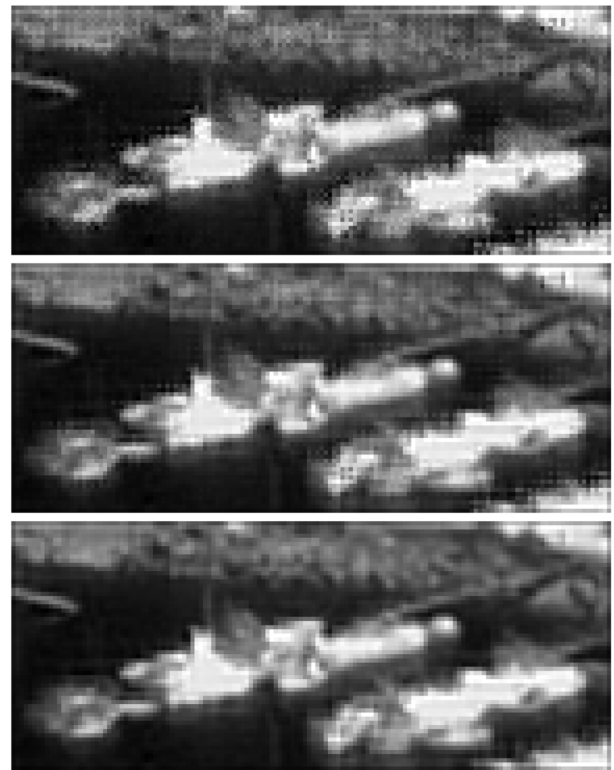


Fig. 21. Reconstructions have been performed using E&F0 (top image), E&F1 (middle image), and TS0 (bottom image) observation model.  $\lambda = 10^{-2}$ .

middle image (E&F1 model). These artifacts are not present in the bottom image (proposed TS0 model). In the same time, comparison of SR results and Fig. 20 shows that resolution has indeed been increased.

VII. CONCLUSION

The presented paper deals with SR techniques in the field of aerial imagery. The proposed work focuses on the observation model in the case of an affine motion whereas the main part of SR literature deals with the inversion process or motion estimation.

We analyzed the existing observation models used in SR reconstruction and emphasized their underlying assumptions, so as to clarify their limitations. As a result, it is shown that these observation models fall into three categories:

- exact computation;
- convolve-then-warp;
- warp-then-convolve.

Exact computation is not tractable for general motions. The convolve-then-warp approach is numerically efficient but is unable to capture large rotations and scale variations. So, only the third approach, due to Elad and Feuer, is relevant in our framework. However, we have observed inaccuracies for rotations as low as  $15^\circ$  and a zooming factor as low as 20%. We succeeded in extending the E&F model to cover a more important range of affine transforms with high accuracy, for about 30% more computation time. The pointwise interpolation stage in the E&F method has been replaced by  $L_2$  functional approximation techniques. This technique combines a two-shear decomposition for the affine transform and a 1-D  $L_2$  projection on a shifted bspline basis.

The proposed model has been compared with various E&F-like models. These models have been associated to several regularization settings to be tested for SR reconstruction purposes using synthetic and real-image sequences.

These tests have stressed the importance of the observation model in SR reconstruction when dealing with large zoom and rotation effects. In particular, the choice of a bilinear interpolation instead of a nearest-neighbor one within an Elad and Feuer setting dramatically improves the reconstructions. Moreover, the proposed model consistently achieves even better results.

Further research should be conducted to accurately deal with homographic motion, or piecewise parametric motion. It should unlock SR techniques to a larger application field.

#### ACKNOWLEDGMENT

This work was performed at ONERA during the Ph.D. work of G. Rochefort. The authors would like to thank É. Thiébaud for providing an implementation of the VMLMB algorithm (see Section IV), used to optimize the constrained regularized criteria.

#### REFERENCES

- [1] R. Tsai and T. Huang, "Multiframe image restoration and registration," *Adv. Comput. Vis. Image Process.*, vol. 1, pp. 317–339, 1984, JAI.
- [2] R. Schultz and R. Stevenson, "Extraction of high-resolution frames from video sequences," *IEEE Trans. Image Process.*, vol. 5, no. 6, pp. 996–1011, Jun. 1996.
- [3] A. Patti, M. Sezan, and A. M. Tekalp, "Superresolution video reconstruction with arbitrary sampling lattices and nonzero aperture time," *IEEE Trans. Image Process.*, vol. 6, no. 8, pp. 1064–1076, Aug. 1997.
- [4] R. C. Hardie, K. J. Barnard, and E. E. Armstrong, "Joint MAP registration and high-resolution image estimation using a sequence of undersampled images," *IEEE Trans. Image Process.*, vol. 6, no. 12, pp. 1621–1633, Dec. 1997.
- [5] M. Elad and A. Feuer, "Restoration of a single superresolution image from several blurred, noisy, and undersampled measured images," *IEEE Trans. Image Process.*, vol. 6, no. 12, pp. 1646–1658, Dec. 1997.
- [6] S. Farsiu, M. Robinson, M. Elad, and P. Milanfar, "Fast and robust multiframe super-resolution," *IEEE Trans. Image Process.*, vol. 13, no. 10, pp. 1327–1343, Oct. 2004.
- [7] S. C. Park, M. K. Park, and M. G. Kang, "Super-resolution image reconstruction: A technical overview," *IEEE Signal Process. Mag.*, vol. 20, no. 3, pp. 21–36, May 2003.
- [8] S. Baker and T. Kanade, "Limits on super-resolution and how to break them," *IEEE Trans. Pattern Anal. Mach. Intell.*, vol. 24, no. 9, pp. 1167–1183, Sep. 2002.
- [9] S. Mann and R. W. Picard, "Virtual bellows: Constructing high quality stills from video," in *Proc. IEEE Int. Conf. Image Processing*, Austin, TX, 1994, pp. 363–367.
- [10] P. Thévenaz, U. Ruttimann, and M. Unser, "A pyramid approach to subpixel registration based on intensity," *IEEE Trans. Image Process.*, vol. 7, no. 1, pp. 27–41, Jan. 1998.
- [11] S. Kim, N. Bose, and H. Valenzuela, "Recursive reconstruction of high resolution image from noisy undersampled multiframe," *IEEE Trans. Acoust., Speech, Signal Process.*, vol. 38, no. 6, pp. 1013–1027, Jun. 1990.
- [12] S. Kim and W. Su, "Recursive high-resolution reconstruction of blurred multiframe images," *IEEE Trans. Image Process.*, vol. 2, no. 4, pp. 534–539, Oct. 1993.
- [13] H. Ur and D. Gross, "Improved resolution from sub-pixel shifted pictures," *CVGIP: Graph. Models, Image Process.*, vol. 2, no. 54, pp. 181–186, Mar. 1992.
- [14] M. Elad and Y. Hel-Or, "A fast super-resolution reconstruction algorithm for pure translational motion and common space-invariant blur," *IEEE Trans. Image Process.*, vol. 10, no. 10, pp. 1187–1193, Oct. 2001.
- [15] B. C. Tom and A. K. Katsaggelos, "Reconstruction of a high-resolution image by simultaneous registration, restoration, and interpolation of low-resolution images," in *Proc. Int. Conf. Image Process.*, Washington, DC, 1995, pp. 2539–2542.
- [16] A. Tekalp, M. Ozkan, and M. Sezan, "High-resolution image reconstruction from lower-resolution image sequences and space-varying image restoration," *IEEE Trans. Acoust., Speech, Signal Process.*, vol. 3, pp. 169–172, Mar. 1992.
- [17] E. Lee and M. Kang, "Regularized adaptive high-resolution image reconstruction considering inaccurate subpixel registration," *IEEE Trans. Image Process.*, vol. 12, no. 7, pp. 526–537, Jul. 2003.
- [18] A. J. Patti and Y. Altunbasak, "Artifact reduction for set theoretic super resolution image reconstruction with edge adaptative constraints and higher-order interpolants," *IEEE Trans. Image Process.*, vol. 10, no. 1, pp. 179–186, Jan. 2001.
- [19] N. Woods, N. Galatsanos, and A. Katsaggelos, "EM-based simultaneous registration, restoration, and interpolation of super-resolved images," in *IEEE Int. Conf. Image Processing*, Barcelona, Spain, 2003.
- [20] R. C. Hardie, K. J. Barnard, J. G. Bognar, E. E. Armstrong, and E. A. Watson, "High-resolution image reconstruction from a sequence of rotated and translated frames and its application to an infrared imaging system," *Opt. Eng.*, vol. 37, no. 1, pp. 247–260, Jan. 1998.
- [21] M. Elad and A. Feuer, "Superresolution restoration of an image sequence: Adaptive filtering approach," *IEEE Trans. Image Process.*, vol. 8, no. 3, pp. 387–395, Mar. 1999.
- [22] S. Lertrattanapanich and N. K. Bose, "High resolution image formation from low resolution frames using delaunay triangulation," *IEEE Trans. Image Process.*, vol. 11, no. 12, pp. 1427–1441, Dec. 2002.
- [23] P. Thévenaz and M. Unser, "Separable least-squares decomposition of affine transformations," presented at the IEEE Int. Conf. Image Processing, Santa Barbara, CA, Oct. 1997.
- [24] J. Idier, "Convex half-quadratic criteria and interacting auxiliary variables for image restoration," *IEEE Trans. Image Process.*, vol. 10, no. 7, pp. 1001–1009, Jul. 2001.
- [25] H. Curry and I. Schoenberg, "On spline distributions and their limits: The polya distribution functions," *Bull. Amer. Math. Soc.*, vol. 53, no. 1114, 1947.
- [26] M. Unser, A. Aldroubi, and M. Eden, "B-spline signal processing: Part I—Theory," *IEEE Trans. Signal Process.*, vol. 41, no. 2, pp. 821–833, Feb. 1993.
- [27] ———, "B-Spline signal processing: Part II—Efficient design and applications," *IEEE Trans. Signal Process.*, vol. 41, no. 2, pp. 834–848, Feb. 1993.
- [28] A. Papoulis, *Signal Analysis*. New York: McGraw-Hill, 1977.
- [29] H. Stark and P. Oskoui, "High-resolution image recovery from image-plane arrays, using convex projections," *J. Opt. Soc. Amer.*, vol. 6, no. 11, pp. 1715–1726, Nov. 1989.
- [30] I. Sutherland and G. Hodgman, "Reentrant polygon clipping," *Commun. ACM*, vol. 17, pp. 32–42, 1974.
- [31] M. Irani and S. Peleg, "Improving resolution by image registration," *Comput. Vis. Graph., Image Process.*, vol. 52, no. 3, pp. 231–239, May 1991.
- [32] E. Catmull and A. Smith, "3D-transformations of images in scanline order," in *Proc. Comput. Graph.*, Jul. 1980, vol. 14, no. 3, pp. 279–285.
- [33] A. Paeth, "A fast algorithm for general raster rotation," in *Proc. Graphics Interface*, 1986, pp. 77–81.
- [34] D. Fraser and R. Schowengerdt, "Avoidance of additional aliasing in multipass image rotations," *IEEE Trans. Image Process.*, vol. 6, no. 3, pp. 721–735, Nov. 1994.
- [35] S. Horbelt, "Spline and Wavelets for Image Warping and Projection," Ph.D. dissertation, Swiss Federal Inst. Technol. Lausanne (EPFL), Lausanne, Switzerland, May 2001.
- [36] A. M. Barrutia, T. Blu, and M. Unser, "Least-squares image resizing using finite differences," *IEEE Trans. Image Process.*, vol. 10, no. 9, pp. 1365–1378, Sep. 2001.
- [37] M. Unser, A. Aldroubi, and M. Eden, "Enlargement or reduction of digital images with minimum loss of information," *IEEE Trans. Image Process.*, vol. 4, no. 3, pp. 247–258, Mar. 1995.
- [38] J. Nocedal and S. J. Wright, *Numerical Optimization*. New York: Springer-Verlag, 1999.
- [39] J. L. Mundy and A. Zisserman, Eds., *Geometric Invariants in Computer Vision*. Cambridge, MA: MIT Press, 1992.
- [40] D. G. Lowe, "Distinctive image features from scale invariant keypoints," *Int. J. Comput. Vis.*, vol. 60, no. 2, pp. 91–110, 2004.



**Gilles Rochefort** was born in Issy les Moulineaux, France, in 1977. He graduated from the École Supérieure de Mécanique et d'Électricité in 2000 and received the Doctorat degree in signal processing from the Université Paris-Sud, Orsay, France, in 2005.

He is a Research Engineer at RealEyes 3D, Saint-Cloud, France, a young company involved in the design of camera phone applications. He is interested in inverse problems in image processing and, more specifically, in improving the image quality of low-cost cameras.

cost cameras.



**Frédéric Champagnat** (M'99) was born in Dakar, Senegal, in 1966. He graduated from the École Nationale Supérieure de Techniques Avancées in 1989 and received the Ph.D. degree in physics from the Université de Paris-Sud, Orsay, France, in 1993.

From 1994 to 1995, he had a Postdoctoral position with the Biomedical Engineering Institute, École Polytechnique, Montreal, QC, Canada. Since 1998, he has been with the Office National d'Études et Recherches Aérospatiales, Châtillon, France. His main interests are in the field of spatio-temporal

processing for space or aerial image sequences, in particular registration, motion estimation, super-resolution, and detection.



**Guy Le Besnerais** was born in Paris, France, in 1967. He graduated from the École Nationale Supérieure de Techniques Avancées in 1989 and received the Ph.D. degree in physics from the Université de Paris-Sud, Orsay, France, in 1993.

Since 1994, he has been with the Office National d'Études et Recherches Aérospatiales, Châtillon, France. His main interests are in the fields of image reconstruction and structure-from-motion and spatio-temporal processing for space and aerial image sequences.



**Jean-François Giovannelli** was born in Béziers, France, in 1966. He graduated from the École Nationale Supérieure de l'Électronique et de ses Applications in 1990 and received the Doctorat degree in physics from the Université Paris-Sud, Orsay, France, in 1995.

He is presently an Assistant Professor in the Département de Physique, Université Paris-Sud, and a Researcher with the Laboratoire des Signaux et Systèmes (CNRS-Supélec-UPS). He is interested in regularization and Bayesian methods for inverse

problems in signal and image processing. His application fields essentially concern astronomical, medical, and geophysical imaging.